Journal of Materials Chemistry A

Facile Strategy for Controllable Synthesis of Stable Mesoporous Black TiO2 Hollow Spheres with Efficient Solar-Driven Photocatalytic Hydrogen Evolution

Journal:	*Journal of Materials Chemistry A*
Manuscript ID	TA-ART-03-2016-001928.R1
Article Type:	Paper
Date Submitted by the Author:	03-Apr-2016

Complete List of Authors:	Hu, Weiyao; Heilongjiang University, Zhou, Wei; Heilongjiang University, Zhang, Kaifu; Heilongjiang University, Zhang, Xiangcheng; Heilongjiang University, Wang, Lei; Heilongjiang University, jiang, baojiang; Heilongjiang University, Tian, Guohui; Heilongjiang University, Key Laboratory of Functional Inorganic Material Chemistry, Ministry of Education of the People's Republic of China, Heilongjiang University Zhao, Dongyuan; Fudan University, Department of Chemistry Fu, honggang; Heilongjiang University,

Journal Name

ARTICLE

Facile Strategy for Controllable Synthesis of Stable Mesoporous Black TiO_2 Hollow Spheres with Efficient Solar-Driven Photocatalytic Hydrogen Evolution

Received 00th January 20xx,
Accepted 00th January 20xx

DOI: 10.1039/x0xx00000x

www.rsc.org/

Weiyao Hu,[a] Wei Zhou,*[a], Kaifu Zhang,[a] Xiangcheng Zhang,[a] Lei Wang,[a] Baojiang Jiang,[a] Guohui Tian,[a] Dongyuan Zhao[b] and Honggang Fu*[a]

The hydrogenated black TiO_2 is confirmed to tune the bandgap and utilize solar energy effectively. Herein, we report a facile strategy for controllably synthesizing stable mesoporous black TiO_2 hollow spheres (MBTHSs) with narrow bandgap *via* a template-free solvothermal approach combined with small amine molecules reflux-encircling process and subsequent high-temperature hydrogenation, which are composed of highly crystalline pore-walls, Ti^{3+} in frameworks and surface disorders. The encircled protectors especially ethylenediamines result in high thermostability of the TiO_2 hollow structures, which not only facilitate hydrogenation (600 °C), but also inhibit grain growth and anatase-to-rutile phase transformation as well as retain a high structural integrity. The MBTHSs with a diameter of ~ 700 nm possess relatively high surface area of ~ 80 $m^2 g^{-1}$, large pore size and pore volume of ~ 12 nm and ~ 0.20 $cm^3 g^{-1}$, respectively. The diameters and wall thicknesses are controllable from ~ 500 nm to 1 μm and ~ 35 to 115 nm, respectively. The high crystallinity, integrated hollow structure, Ti^{3+} in frameworks and surface disorders of the MBTHSs give rise to extending photoresponse from ultraviolate to visible light region and the significant improvement for solar-driven photocatalytic hydrogen evolution rate (241 μmol h^{-1} 0.1 g^{-1}), which is two times as high as that of the black TiO_2 nanoparticles (118 μmol h^{-1} 0.1 g^{-1}) and almost three times for pristine mesoporous TiO_2 hollow spheres (81 μmol h^{-1} 0.1 g^{-1}), respectively.

Introduction

Mesoporous TiO_2 hollow spheres have recently attracted increasing research interests because of their specific features, such as low density, high surface-to-volume ratio, the effect of void space, high shell permeability, excellent electronic and optical properties, and widespread applications in fields of photocatalysis, solar cells, photoelectrochemical water splitting, drug delivery, sensors and energy storage.[1-6] Significant efforts have been made to fabricate various mesoporous TiO_2 hollow spheres as photocatalysts, and their performance indeed enhanced obviously.[7-9] Usually, the synthesis approach includes templating and template-free methods.[10-12] The template-based synthesis benefits for great versatility for various hollow structures, but creating uniform coatings on the corresponding templates and removing them is quite complicated.[13,14] What's worse, the hollow structures could be easily collapsed during removal of templates. Although template-free approach leaves out the complex multi-step synthetic procedures, it is difficult to controllably synthesize uniform mesoporous TiO_2 hollow spheres, such as tunable diameter, wall thickness, pore size, *etc*. Moreover, the large bandgap of anatase TiO_2 (~ 3.2 eV) greatly limits the efficiency of solar-driven photocatalysis, because the light absorption is only confined in ultraviolet (UV) region, which represents a small fraction of solar energy.[15,16]

The recent discovery of black TiO_2 nanoparticles by Mao and coworkers via hydrogenation has triggered huge splash and opened a new epoch for utilizing long-wavelength light.[17] Some proposals including both theoretical computations and experiments are employed to reveal the black TiO_2 materials, such as surface disorder-engineered layer, Ti^{3+} (oxygen vacancy), and hydrogen plasma, which could rationally explain these phenomena and represent a big breakthrough in photocatalysis.[18-25] Santo and coworkers found that the synergistic effect of oxygen vacancies and surface disorder resulted in narrowing the bandgap of black TiO_2 nanoparticles.[26] Scrosati and coworkers showed that the presence of trivalent Ti reduced the bandgap energy as low as 1.8 eV.[27] Very recently, Yang and coworkers have revealed the physical origin of the Ti^{3+} related photoabsorption and visible light photocatalytic activity in TiO_2 *via* two-photon photoemission spectroscopy and density functional theory calculation, which led to a better understanding of the mechanism for the enhanced long-wavelength light

a Key Laboratory of Functional Inorganic Material Chemistry, Ministry of Education of the People's Republic of China, Heilongjiang University, Harbin 150080, P. R. China. E-mail: fuhg@vip.sina.com, zwchem@hotmail.com
b Department of Chemistry, Laboratory of Advanced Materials, Shanghai Key Lab of Molecular Catalysis, iChEM and Innovative Materials, and State Key Laboratory of Molecular Engineering of Polymers, Fudan University, Shanghai 200433, P. R. China

Electronic Supplementary Information (ESI) available: Additional XRD, Raman, SEM, N_2 adsorption, XPS, SAED and SPS. See DOI: 10.1039/x0xx00000x

absorption.[28] Although the solar-driven photocatalytic performance of the current black TiO_2 materials is indeed state-of-the-art up to now, it is still far from desirable. Mesoporous black TiO_2 hollow spheres would be ideal candidates for further improving the solar-driven photocatalytic performance because the unique hollow structures are beneficial for efficient light utilization and offering more surface active sites. However, the conventional mesoporous TiO_2 hollow spheres are easily collapsed during high-temperature treatment process due to the low thermal stability,[29,30] which is a major obstacle for effective surface hydrogenation, because the frameworks could be collapsed easily due to the capture of oxygen by hydrogen during the high-temperature hydrogenation process. Therefore, it is still a great challenge for controllably fabricating stable mesoporous black TiO_2 hollow spheres.

Herein, we demonstrate a facile route to synthesize stable mesoporous black TiO_2 hollow spheres (MBTHSs) with controllable diameters and wall thicknesses through template-free solvothermal approach combined with small amine molecules encircling strategy and atmospheric hydrogenation (Scheme 1). Our synthesis system is suitable for efficient encircling of these small amine molecules on the surface of the mesoporous TiO_2 hollow spheres (MTHSs), in which the hollow structures and anatase phase can be maintained up to 900 °C. The highly-thermostable MTHSs are good candidate for subsequent high-temperature hydrogenation. The obtained MBTHSs possess a relative high surface area of ~ 80 $m^2 g^{-1}$, and a large pore size of ~ 12 nm. The diameters and wall thicknesses are controlled from ~ 500 nm to 1 μm and ~ 35 to 115 nm, respectively. Moreover, the MBTHSs extend the photoresponse from UV to visible light region and exhibits a high solar-driven photocatalytic hydrogen evolution rate (241 μmol h^{-1} 0.1 g^{-1}), which is almost three times as high as that of pristine MTHSs (81 μmol h^{-1} 0.1 g^{-1}). The MBTHSs will be an excellent host material to form novel heterojunction composites through the growth of a variety of narrow band-gap semiconductors, noble metals with surface plasmon resonance, and the assembly of functional heterogeneous components in the mesoporous channels or cavity, and will have widespread applications in fields of energy and environment.

Experimental Section

Chemicals

Tetrabutyl titanate (TBOT), N,N-dimethylformamide (DMF), ethanol (EtOH), ethylenediamine, hexamethylenetetramine, n-butylamine, isopropylamine, trimethylamine, ammonium hydroxide, methanol and KOH were of analytical grade and purchased from Tianjin Kemiou Chemical Reagent Co., Ltd. Anhydrous oxalic acid and anatase TiO_2 nanoparticles (25 nm) were purchased from Aladdin Industrial Inc. All chemicals were used as received without further purification. Deionized water was used for all experiments.

Synthesis of the stable mesoporous black TiO_2 hollow spheres.

In a typical, 0.1 g of tetrabutyltitanate (TBOT) and 7.25 g of anhydrous oxalic acid were dissolved in 65 mL of N, N-dimethylformamide. Then, transferred to a 100-mL autoclave and heated to 170 °C for 10 h. The as-synthesized samples were washed with ethanol and dried at 60 °C for 6 h. Subsequently, the products were refluxed with ethylenediamine aqueous solution (pH 11~12) for 48 h at 80-90 °C. The obtained powders were washed by deionized water several times and dried at 60 °C overnight. Finally, the resulting samples were calcined at 600 °C for 3 h in air to remove the organic species and improve crystallinity, with the temperature ramping rate of 5 °C min^{-1}. The white mesoporous TiO_2 hollow spheres were obtained (denoted as MTHSs). Before being calcined in H_2 flow at 600 °C for 3 h under normal pressure conditions, with a constant heating rate of 10 °C min^{-1}, it was deaerated under inert gas flow (N_2) for 0.5 h. Finally, the stable mesoporous black TiO_2 hollow spheres were obtained (denoted as MBTHSs). In order to confirm the encircling strategy, several other small molecule amines and ammonium hydroxide were chosen for proving the effect of high thermostability, including trimethylamine, isopropylamine, n-butylamine and hexamethylenetetramine. As comparative test, commercial anatase TiO_2 nanoparticles were also calcined in H_2 flow under the same conditions, and finally the black TiO_2 nanoparticles were obtained. The MBTHSs with different diameters were synthesized *via* adjusting the amount of TBOT (0.06, 0.08, 0.10, 0.12, 0.14 and 0.16 g, respectively), keeping other synthesis parameters constant. The MBTHSs with various wall thicknesses were also prepared through tuning solvothermal reaction time (8, 9, 10, 11 and 12 h).

Characterizations

X-ray diffraction (XRD) patterns were obtained by a Bruker D8 Advance diffractometer by using Cu Kα radiation (λ = 1.5406 Å, 40 kV, 40 mA). The scan rate and the step size were 6 ° min^{-1} and 0.02 °, respectively. Raman measurements were performed with a JobinYvon HR 800 micro-Raman spectrometer at 457.9 nm. The laser beam was focused with a 50 × objective lens to a ca. 1 μm spot on the surface of the sample. Scanning electron microscopy (SEM) micrographs were obtained with a Philips XL-30-ESEM-FEG instrument operating at 20 kV. The transmission electron microscopy (TEM) experiments were performed on a JEOL JEM-2100 F microscope (Japan) operated at 200 kV. Carbon-coated copper grids were used as the sample holders. X-ray photoelectron spectroscopy (XPS, Kratos, ULTRA AXIS DLD) was carried out with monochrome Al Kα (hν = 1486.6 eV) radiation. All binding energies were calibrated by referencing to C 1s peak at 284.6 eV. Diffuse reflectance spectroscopy (DRS) was measured on a UV/vis spectrophotometer (Shimadzu UV-2550) in the range of 200-800 nm. The bandgaps were estimated by extrapolating a linear part of the plots to $(\alpha h\nu)^2 = 0$. Nitrogen adsorption-desorption isotherms at 77 K were collected on an AUTOSORB-1 (Quantachrome Instruments) nitrogen adsorption apparatus. All of the samples were degassed under vacuum at 180 °C for

at least 8 h prior to measurement. The Brunauer–Emmett–Teller (BET) equation was used to calculate the specific surface area. Pore size distributions were obtained using the Barrett–Joyner–Halenda (BJH) method from the adsorption branch of the isotherms. The surface photovoltage spectroscopy (SPS) measurements were carried out with a home-built apparatus equipped with a lock-in amplifier (SR830) synchronized with a light chopper (SR540). The powders were sandwiched between two indium tin oxide (ITO)-coated glass electrodes, and monochromatic light was passed from a 500 W xenon lamp through a double prism monochromator (SBP300). Scanning Kelvin probe (SKP) measurements (SKP5050 system, Scotland) were performed at normal laboratory conditions (in ambient atmosphere). A gold electrode was used as the reference electrode. The electron paramagnetic resonance (EPR) spectra were measured at room temperature with an EPR spectrometer (JES-FA 300, 9.4 GHz, 1 mW).

Photocatalytic hydrogen evolution

The photocatalytic hydrogen evolution experiments were conducted in an online photocatalytic hydrogen generation system (AuLight, Beijing, CEL-SPH2N) at ambient temperature (20 °C). Photocatalyst (100 mg) loaded with Pt (1 wt.%) was suspended in a mixture of 80 mL of water and 20 mL of methanol in closed-gas circulation reaction cell by using a magnetic stirrer. Prior to the reaction, the mixture was deaerated by evacuation to remove O_2 and CO_2 dissolved in water. An AM 1.5 solar power system (solar simulator (Oriel, USA) equipped with an AM 1.5G filter (Oriel, USA)) was used as light irradiation source. Gas evolution was observed only under photoirradiation with a power density of 100 mW cm^{-2}, being analyzed by an on-line gas chromatograph (SP7800, TCD, molecular sieve 5 Å, N_2 carrier, Beijing Keruida Limited). The determination of the apparent quantum efficiency for hydrogen generation was performed using the same closed circulating system under illumination of a 300 W Xe lamp with bandpass filter (365, 420 and 520 nm) system. Once the photocatalytic reaction of a testing cycle in 3 h was complete, the reactor was replenished with 1 mL of methanol and degassed in vacuum before starting the subsequent cycle.

Photoelectrochemical property

The photoelectrochemical properties were carried out using a Princeton Versa STAT 3 in a standard three electrode configurations with MBTHSs and MTHSs materials used as photoanodes, Pt foil as counter electrode, and Ag/AgCl electrode as the reference electrode. The photoanodes were prepared by traditional spray coating method, using a glass rod to roll a paste containing 0.2 g of powders and 0.5 mL of EtOH on transparent conducting glass (TCO, fluorine doped SnO_2 layer, 20 Ω/square, Nippon sheet glass, Japan), and pressed at 1000 kg cm^{-2} between stainless-steel plates in a hydraulic press using aluminium foil to prevent adhesion to form a film (2 × 1 cm), then calcination at 350 °C under N_2 atmosphere with a constant heating rate of 10 °C min^{-1}. 1 M KOH purged with N_2 was used as the electrolyte. An AM 1.5 solar power system (Oriel, USA) was used as light irradiation source.

Results and discussion

After surface hydrogenation at 600 °C, the X-ray diffraction (XRD) patterns of both MBTHSs and MTHSs (Fig. 1A) show five obvious crystal peaks at 2θ = 25.2-55.2 °, which could be indexed as the 101, 004, 200, 105, and 211 inflections for anatase phase (JCPDS, No.21-1272), but the intensity for the former decreases and broadens evidently, indicating that its crystalline structure has some variation after hydrogenation. The structural changes are further investigated by Raman technique (Fig. 1B). Five peaks at 149, 199, 393, 513, and 639 cm^{-1} could be ascribed to typical anatase Raman bands of E_g, E_g, B_{1g}, A_{1g} (B_{1g}), and E_g modes, respectively.[31,32] Remarkably, the obvious shift of these bands for MBTHSs demonstrates that the original symmetry of TiO_2 lattice is destroyed after hydrogenation. The lattice disorder in TiO_2 could yield midgap states, which would form a continuum with the conduction band edge and lead to band tail states merging with the valence band, and thus narrowing the bandgap.[33,34]

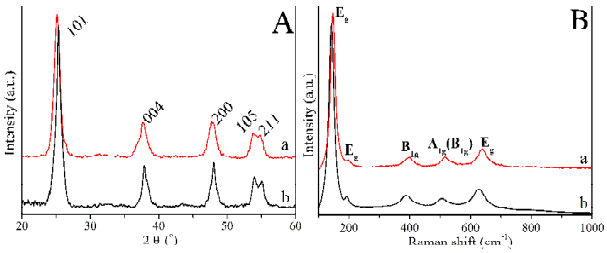

Fig. 1 Typical XRD patterns (A) and Raman spectra (B) of the stable mesoporous black TiO_2 hollow spheres after hydrogen gas annealing at 600 °C for 3 h (a) and stable mesoporous TiO_2 hollow spheres after being calcined in air at 600 °C for 3 h (b).

The scanning electron microscopy (SEM) and transmission electron microscopy (TEM) images both show mesoporous TiO_2 hollow spheres with the diameters of ~ 700 nm after H_2 annealing treatment (Fig. 2a, b). The mesopores can be observed obviously (inset of Fig. 2b). High-resolution TEM image (Fig. 2c) clearly shows that the pore-walls consist of highly crystalline TiO_2 nanoparticles. The lattice fringes with d-spacing of 0.35 nm are clearly observed (Fig. 2c), which well corresponds to (101) crystallographic planes of anatase. Well-resolved diffraction rings of selected-area electron diffraction (SAED) pattern (Fig. S1) further confirm the high crystallinity of the stable mesoporous black TiO_2 hollow spheres. By comparison with the stable mesoporous TiO_2 hollow spheres (Fig. 2d, e), the hollow structures nearly keep constant after high-temperature hydrogenation. Furthermore, compared to MTHSs with high crystallinity (Fig. 2f), a thin disordered surface layer encircling the crystalline core could be observed clearly (Fig. 2c), indicating that the surface hydrogenation is efficient. N_2 adsorption/desorption isotherms of MTHSs and MBTHSs both show typical type IV curves (Fig. S2), indicating

mesoporous materials[35]. The specific Brunauer-Emmett-Teller surface area and pore size are slightly varied after hydrogenation, in which the surface area, pore size and pore volume for MBTHSs are ~ 80 $m^2 g^{-1}$, ~ 12 nm and ~ 0.20 $cm^3 g^{-1}$, respectively, indicating that the hollow structure retains well during the high-temperature H_2 annealing treatment, which is in good agreement with SEM and TEM observation. Diffuse reflectance measurements reveal that the bandgap is reduced after hydrogenation, because an obvious shift in the onset of absorption from UV to visible light region can be observed (Fig. 2g), along with the color change from white to black (inset of Fig. S3). The bandgap for MBTHSs is about 2.59 eV (Fig. S3), smaller than that of MTHSs (~ 3.17 eV), which maybe substantially enhance the solar-driven photocatalytic activity.

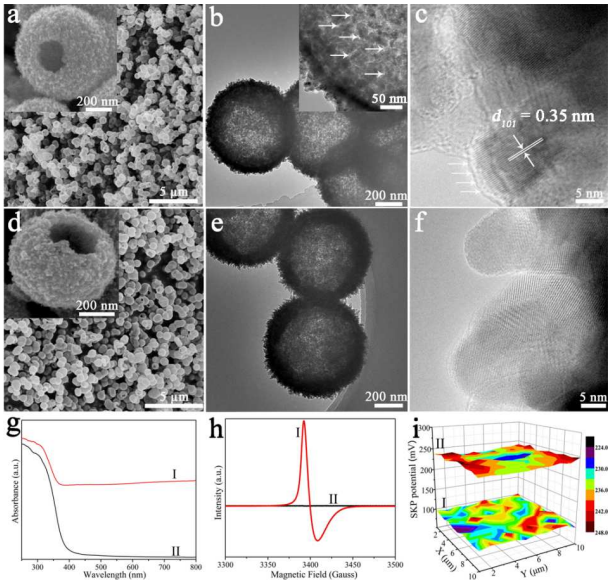

Fig. 2 SEM and TEM images of the stable mesoporous black TiO_2 hollow spheres (a, b, c) after hydrogen gas annealing at 600 °C for 3 h and the stable mesoporous TiO_2 hollow spheres (d, e, f) after being calcined in air at 600 °C for 3 h. The ultraviolet-visible absorption spectra (g), electron paramagnetic resonance spectroscopy (h) and scanning Kelvin probe maps (i) of the stable mesoporous black TiO_2 hollow spheres (I) and stable mesoporous TiO_2 hollow spheres (II). The white arrows in the inset of (b) point to mesopores.

The wall thickness of MBTHSs, which plays vital role for photocatalysis, is controllable from ~ 35 to 115 nm via adjusting the reaction time (Fig. 3). With increasing the reaction time, the wall thickness gradually becomes thinner due to the further Ostwald ripening process. The wall thickness is only ~ 35 nm when the reaction time is up to 12 h. Continue to prolong the reaction times, the hollow spheres begin to collapse. Moreover, the diameter of MBTHSs is also controllable through tuning the amounts of Ti precursors. The diameters of black TiO_2 hollow spheres are controlled easily from ~ 500 nm to 1 μm with increasing the amount of Ti precursors (Fig. S4). The hydrolysis-condensation of Ti precursors can produce Ti (IV) nanoclusters, and the different spatial configurations derived from their dimensions and linearities can modulate the hybrid interface, and thus lead to hollow structures with different diameters during Ostwald ripening process. The different sizes for hollow spheres are closely related to the photocatalytic performance because of the different surface areas and active sites. The surface areas decrease remarkably with increasing the diameters. So, controllable diameters of MBTHSs are important for photocatalysis.

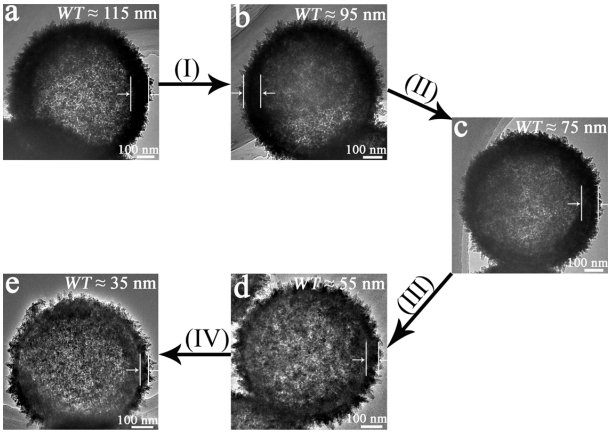

Fig. 3 The wall thicknesses (WT) evolution of the stable mesoporous black TiO_2 hollow spheres with different solvothermal reaction times (a: 8 h; b: 9 h; c: 10 h; d: 11 h; e: 12 h).

X-ray photoelectron spectroscopy (XPS) is conducted to investigate the surface states of MBTHSs and MTHSs. The Ti 2p spectra are almost identical for both of them (Fig. S5A). These features are identical with Ti 2p3/2 and 2p1/2 centered at 458.3 and 464.2 eV, which are all assigned to Ti^{4+} and indicate that no Ti^{3+} species exist on the surface[36,37]. Usually, the surface Ti^{3+} is unstable in air as it is easily oxidized by air or dissolved oxygen in water[38]. The XPS technique could only limit to characterize the top several nanometers surface layer of the nanomaterials, which could not obtain the information in the bulk. The O 1s spectrum of MBTHSs is different from that of MTHSs obviously. The former exhibits a broad O 1s peak with a strong shoulder at high binding energy, which can be deconvoluted into two peaks centered at 529.5 and 531.3 eV. The broader peak at 531.3 eV could be attributed to Ti-OH species, implying the formation of more hydroxyl groups on TiO_2 surface after hydrogenation (Fig. S5B)[39]. The valence band XPS for MTHSs displays typical valence band characteristics of anatase TiO_2, with the edge of the maximum energy at ~ 2.41 eV (Fig. S5C). While the valence band maximum (VBM) energy for MBTHSs blue-shifts toward to the vacuum level at ~ 1.72 eV, further illustrating the efficient surface hydrogenation. Combined with the TEM analyses, the surface lattice disorder (e.g. Ti-H, O-H) can blue-shift the VBM of TiO_2 through introducing midgap states which would be introduced *via* the formation of Ti^{3+} or oxygen vacancy, meanwhile, the conduction band minimum is almost unchanged[40,41].

Therefore, the bandgap of anatase TiO_2 is reduced after hydrogenation, which is in good agreement with the diffuse reflectance measurements. Electron paramagnetic resonance (EPR) spectra were recorded at room temperature to determine the presence of Ti^{3+} in the bulk. An obvious EPR signal for MBTHSs could be observed at g ≈ 1.98 (Fig. 2h), which should be assigned to Ti^{3+} resulted from the reduction of H_2 and confirmed the presence of Ti^{3+} in MBTHSs[42-46]. Combined with the XPS results, Ti^{3+} species are not present on the surface but mainly located in the bulk, which is crucial for the stability of MBTHSs and responsible for the narrow bandgap. The scanning Kelvin probe (SKP) is sensitive to discern subtle molecular interactions via vibrating electromagnetic and acoustic fields, which shows relative flat potential change according to work function[47-49]. The SKP images present the direct evidence for potential change. The work-function for MBTHSs (~ 5.19 eV) is lower than that of MTHSs (~ 5.34 eV), which ensures the easier escape of electrons from the former and then to the cocatalysts for photocatalytic hydrogen evolution (Fig. 2i). According to SKP results, the approximate Fermi level of MBTHSs is higher than that of MTHSs, which changes the built-in electric field and surface band bending[50,51]. It could accelerate the photogenerated electrons transfer to the surface and then to the cocatalysts, thus greatly reduce the electron-hole recombination and improve the photocatalytic performance.

To validate the effective strategy for controllable fabrication of MBTHSs, a series of control experiments were conducted. Highly-thermostable MTHSs are firstly fabricated via solvothermal approach combined with small amine molecules encircling strategy (Scheme 1), which is chosen as the candidate for the subsequent high-temperature hydrogenation (600 °C). Then, the stable hollow structure frameworks can withstand the subsequent high-temperature calcination (600 °C) and hydrogenation without collapse. Ethylenediamine, which is a representation of small amine molecules for this encircling strategy, plays vital role for the high thermostable mesoporous TiO_2 hollow spheres. The highly-thermostable hollow frameworks facilitate H_2 gas diffusion into TiO_2 and interaction with the frameworks as well as maintain the integrated hollow structures. Ordered mesoporous black TiO_2 had been successfully synthesized via ethylenediamine encircling strategy previously, which offers ideas for preparing stable mesoporous black TiO_2 hollow spheres[23]. Without the pre-treatment, the hollow structure can be collapsed after high-temperature calcination (Scheme 1). Furthermore, the diameters and wall thicknesses are also tunable via adjusting experimental parameters. The specific structure parameters of the stable MTHSs after being calcined at different temperatures are shown in Fig. S6-S10, and Table S1-S2. It is well-known that the crystal phase and crystallization of anatase TiO_2 are intimately associated with calcination temperature. The XRD patterns of the thermostable MTHSs after being calcined at different temperatures are shown in Fig. S6. Five high-intensity peaks for anatase phase (JCPDS, No.21-1272) can be observed. When the calcination temperature is up to 900 °C, the trace rutile is present. However, without ethylenediamine encircling treatment, the rutile phase is present at 700 °C, suggesting that the ethylenediamines indeed improve the crystallinity of anatase and retard the phase transformation from anatase to rutile. These results are consistent very well with the Raman characterization (Fig. S7). N_2 adsorption/desorption isotherms of MTHSs with different calcination temperatures (Fig. S8) all show typical type IV isotherms, and the main pore size distributions are relative narrow (~ 10 nm). It is interesting to note that the specific BET surface area decreases slightly with increasing the calcination temperature after ethylenediamine encircling treatment (Table S1). Conversely, without encircling treatment, it decreases sharply, further indicating the efficient encircling effect. From the SEM images, we can clearly see that the integrated hollow structure could be retained up to 900 °C after ethylenediamine encircling treatment, but very large TiO_2 nanoparticles can be observed without the treatment (Fig. S9). The above results all confirm that the ethylenediamine encircling strategy inhibits the grain growth and anatase-to-rutile phase transformation as well as maintains the high structural integrity of hollow spheres. The high thermostable MTHSs could provide availability for the subsequent surface hydrogenation. After surface hydrogenation at 600 °C, MBTHSs could be obtained successfully and the hollow structure was retained well, which favors utilizing solar energy efficiently and thus improving the photocatalytic performance. Furthermore, a series of small amine molecules, such as trimethylamine, isopropylamine, n-butylamine, *etc*. and ammonium hydroxide, are selected as encircled protectors and similar effects can be obtained, in which the surface bonded N-containing species and textual properties (Fig. S10, Table S2) could be observed clearly, indicating the efficient protection of these small amine molecules or ammonium hydroxide. It also confirms that the encircling strategy is universal approach for preparing highly-thermostable mesoporous TiO_2 hollow spheres. After surface hydrogenation, the anatase phase and integrated hollow structures retain well (Fig. S11).

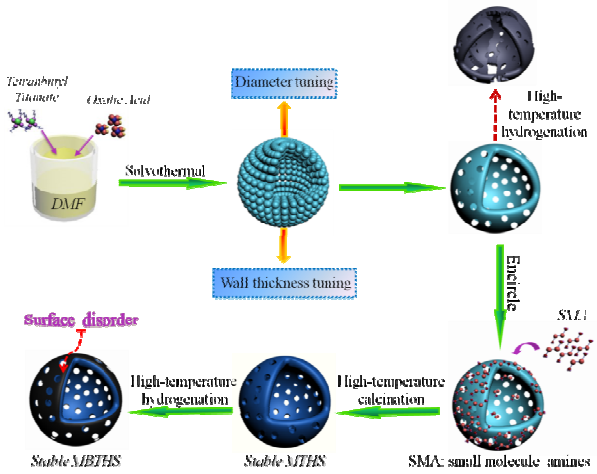

Scheme 1 Schematic illustration of controllable synthesis of the stable mesoporous black TiO_2 hollow spheres.

The MBTHSs were evaluated as photocatalytic hydrogen evolution and exhibited higher photocatalytic activity with the reaction rate of 241 μmol h^{-1} 0.1 g^{-1} than that of MTHSs (81 μmol h^{-1} g^{-1}) under AM 1.5 (Fig. 4A). After testing for six circles, both of them are still persistent nearly constant hydrogen evolution capability, indicating the high stability of the hollow structures. Obviously, the photocatalytic hydrogen evolution rate of 365 nm for MBTHSs is much higher than that of 420 and 520 nm (Fig. 4B), indicating that the main contributor for the high photocatalytic performance is still UV light. To testify the solar energy conversion efficiency, the apparent quantum efficiency (QE) for different single wavelengths is measured, and found to be 72 and 51 % for MBTHSs and MTHSs at 365 nm (Fig. 5B), respectively, implying the higher utilization ratio of photogenerated charges for the former. In visible light region, MBTHS still present photocatalytic activity, and the QE is up to ~ 4 and 3 % at 420 and 520 nm, respectively (Fig. 4B). The results clearly indicate that MBTHSs exhibit high photocatalytic hydrogen evolution both under AM 1.5 and visible light, suggesting that hydrogenation narrows the bandgap and favors the separation of photogenerated electron-hole pairs, which is demonstrated by the surface photovoltage spectroscopy (SPS) analysis (Fig. S12), a well-established noncontact technique for the photophysical processes of semiconductors[52]. A strong SPS peak at around 350 nm for both of them can be observed clearly, which is attributed to the electron transitions from the valence to conduction band (band-to-band transitions, O_{2p}-Ti_{3d})[52]. The strong photovoltage intensity for MBTHSs illustrates their high-efficiency of photogenerated electron-hole pairs and long excitation lifetimes. What's more, the onset of MBTHSs is red-shifted obviously, suggesting the visible light photoactive. Furthermore, compared to MBTHSs, the crushed ones (106 μmol h^{-1} 0.1 g^{-1}) and black TiO_2 nanoparticles (118 μmol h^{-1} 0.1 g^{-1}) exhibit poorer photocatalytic activity under AM 1.5 (Fig. S13), indicating that the hollow structures indeed increase the solar light utilization due to several times refraction of light within the hollow structures. Furthermore, the photocatalytic hydrogen evolution of MBTHSs with different pre-treatment exhibits better photocatalytic performance than that of untreated one (Fig. S14). Moreover, without Pt as a cocatalyst or methanol as a sacrificial agent, the MBTHSs materials still show superior photocatalytic performance to MTHSs, even

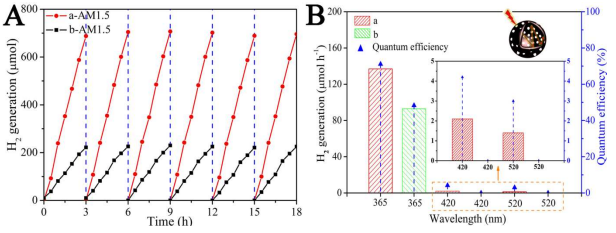

Fig. 4 Photocatalytic hydrogen evolution of the mesoporous black TiO_2 hollow spheres (a) and mesoporous TiO_2 hollow spheres (b). (A) Cycling tests of photocatalytic hydrogen evolution under AM 1.5. (B) The photocatalytic hydrogen evolution rates under single-wavelength light and the corresponding apparent quantum efficiency (QE). The inset of B enlarges the QE of single-wavelength light at 420 and 520 nm. (0.1 g catalysts)

both the hydrogen production rates are ultralow (Fig. S15). Obviously, ethylenediamine, as a representation of small amine molecules for this encircling strategy, is the most ideal candidate for preparing MBTHSs due to the highest photocatalytic activity. In addition, the photocatalytic activity for various wall thicknesses and diameters of MBTHSs is also different (Table S3-S4). Apparently, the MBTHSs with a wall thickness of ~ 75 nm and a diameter of ~ 700 nm possess the best photocatalytic activity.

The photoelectrochemical properties of MBTHSs photoanodes were performed. Linear sweeps voltammogram shows the much higher photocurrent density for MBTHSs (about twice) under AM 1.5 than that of MTHSs (Fig. 5A), illustrating the higher efficient separation of photogenerated charges. The chronoamperometry responses at 0.6 V are nearly constant for both of them indicate the high stability (Fig. 5B), but the photocurrent density is higher for MBTHSs obviously, which is an indication of more efficient charge separation and transport in the sample. The electrochemical impedance measurements show the smaller interfacial resistance for MBTHSs (Fig. 5C), indicating the efficient charge separation by reducing the recombination of electron-hole pairs for MBTHSs. A positive slope in the Mott-Schottky (M-S) plots (Fig. 5D) is a direct evidence of *n*-type semiconductor behavior for both MTHSs and MBTHSs[53]. Furthermore, a shallower slop for MBTHSs could be obtained compared to MTHSs, suggesting an increase of donor density after hydrogenation[54]. Carrier density can be calculated from the corresponding slop according to equation (1)[55].

$$N_d = \frac{2/e_0\varepsilon\varepsilon_0}{d\left(1/C^2\right)/dV} \qquad (1)$$

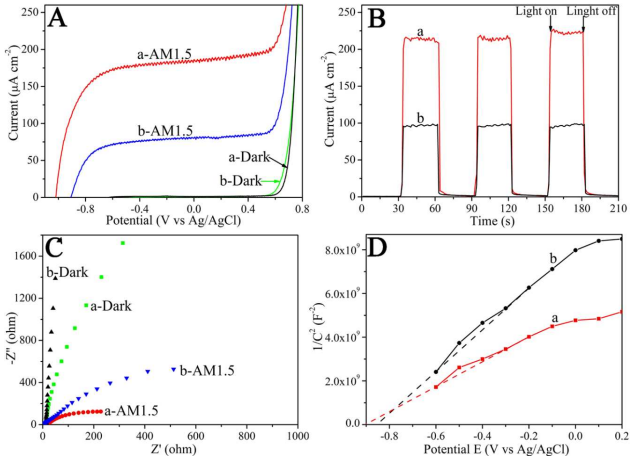

Fig. 5 Photoelectrochemical properties of the stable mesoporous black TiO_2 hollow spheres (a) and stable mesoporous TiO_2 hollow spheres (b). (A) Linear sweeps voltammograms in the dark and under AM 1.5, (B) the chronoamperometry under AM 1.5, (C) the Nyquist plots of

electrochemical impedance in the dark and under AM 1.5, and (D) the Mott-Schottky plots.

We take ε = 55 for anatase TiO_2[56]. The electron densities of MBTHSs and MTHSs are ~ 5.2 × 10^{18} and 2.9 × 10^{18} cm^{-3}, respectively. The increased carrier density for MBTHSs, which is ascribed to the presence of Ti^{3+} and surface disordered layer, gives rise to a better electron-hole pairs separation and transport, and would be responsible for the high photocatalytic hydrogen evolution.

Conclusions

In summary, we have demonstrated the solvothermal approach combined with small amine molecules encircling strategy for the controllable fabrication of the stable MBTHSs with highly crystalline pore-walls and the surface disorders. The highly-themostable hollow frameworks could withstand the subsequent high-temperature hydrogenation (600 °C) without collapse because of the stabilizing effect for small amine molecules encircling strategy. High-temperature hydrogenation introduced a disordered shell on the outside of crystalline TiO_2 core, while Ti^{3+} dispersed in hollow structure frameworks. They were responsible for the long-wavelength light absorption of MBTHSs and the efficient separation of photogenerated electron-hole pairs. The solar-driven hydrogen evolution rate of MBTHSs (241 μmol h^{-1} 0.1 g^{-1}) is several times higher than that of MTHSs (81 μmol h^{-1} 0.1 g^{-1}) and black TiO_2 nanoparticles (118 μmol h^{-1} 0.1 g^{-1}). The newly developed MBTHSs are excellent host materials to form novel heterojunction composites to further improve the photocatalytic performance. The simple and effective approach also provides a promising strategy for improving the photocatalytic performance of other existing semiconductor oxides.

Acknowledgements

We gratefully acknowledge the support of this research by the National Natural Science Foundation of China (21371053, 21376065, 21401048), and International Science & Technology Cooperation Program of China (2014DFR41110).

Notes and references

1 G. Zhang, H. B. Wu, T. Song, U. Paik and X. W. Lou, *Angew. Chem. Int. Ed.*, 2014, **53**, 12590-12593.
2 S. Lee, J. Lee, S. H. Hwang, J. Yun and J. Jang, *ACS Nano*, 2015, **9**, 4939-4949.
3 M. Chen, C. Ye, S. Zhou and L. Wu, *Adv. Mater.*, 2013, **25**, 5343-5351.
4 H. Wang, M. Miyauchi, Y. Ishikawa, A. Pyatenko, N. Koshizaki, Y. Li, L. Li, X. Li, Y. Bando and D. Golberg, *J. Am. Chem. Soc.*, 2011, **133**, 19102-19109.
5 X. Lai, J. E. Halpert and D. Wang, *Energy Environ. Sci.*, 2012, **5**, 5604-5618.
6 H. Ren, J. J. Sun, R. B. Yu, M. Yang, L Gu, P. R. Liu, H. J. Zhao, D. Kisailuse and D. Wang, *Chem. Sci.*, 2016, **7**, 793–798
7 H. Li, Z. Bian, J. Zhu, D. Zhang, G. Li, Y. Huo, H. Li and Y. Lu, J. *Am. Chem. Soc.*, 2007, **129**, 8406-8407.
8 J. B. Joo, Q. Zhang, I. Lee, M. Dahl, F. Zaera and Y. Yin, *Adv. Funct. Mater.*, 2012, **22**, 166-174.
9 H. Liu, J. B. Joo, M. Dahl, L. Fu, Z. Zeng and Y. Yin, *Energy Environ. Sci.*, 2015, **8**, 286-296.
10 L. Li, S. Zhou, E. Chen, R. Qiao, Y. Zhong, Y. Zhang and Z. Li, *J. Mater. Chem. A*, 2015, **5**, 2234-2241.
11 L. Cao, D. Chen and R. A. Caruso, *Angew. Chem. Int. Ed.*, 2013, **52**, 10986-10991.
12 J. H. Pan, X. Z. Wang, Q. Huang, C. Shen, Z. Y. Koh, Q. Wang, A. Engel and D. W. Bahnemann, *Adv. Funct. Mater.*, 2014, **24**, 95-104.
13 H. Ren, R. Yu, J. Wang, Q. Jin, M. Yang, D. Mao, D. Kisailus, H. Zhao and D. Wang, *Nano Lett.*, 2014, **14**, 6679-6684.
14 J. B. Joo, M. Dahl, N. Li, F. Zaera and Y. Yin, *Energy Environ. Sci.*, 2013, **6**, 2082-2092.
15 J. Schneider, M. Matsuoka, M. Takeuchi, J. Zhang, Y. Horiuchi, M. Anpo and D. W. Bahnemann, *Chem. Rev.*, 2014, **114**, 9919-9986.
16 L. Jing, W. Zhou, G. Tian and H. Fu, *Chem. Soc. Rev.*, 2013, **42**, 9509-9549.
17 X. Chen, L. Liu, P. Y. Yu and S. S. Mao, *Science*, 2011, **331**, 746-750.
18 X. Chen, L. Liu and F. Huang, *Chem. Soc. Rev.*, 2015, **44**, 1861-1885.
19 Z. Wang, C. Yang, T. Lin, H. Yin, P. Chen, D. Wan, F. Xu, F. Huang, J. Lin, X. Xie and M. Jiang, *Adv. Funct. Mater.*, 2013, **23**, 5444-5450.
20 J. Cai, Y. Zhu, D. Liu, M. Meng, Z. Hu and Z. Jiang, *ACS Catal.*, 2015, **5**, 1708−1716.
21 X. Chen, L. Liu, Z. Liu, M. A. Marcus, W. Wang, N. A. Oyler, M. E. Grass, B. Mao, P. Glans, P. Y. Yu, J. Guo and S. S. Mao, *Sci. Rep.*, 2013, **3**, 1510.
22 S. Hoang, S. P. Berglund, N. T. Hahn, A. J. Bard and C. B. Mullins, *J. Am. Chem. Soc.*, 2012, **134**, 3659-3662.
23 W. Zhou, W. Li, J. Wang, Y. Qu, Y. Yang, Y. Xie, K. Zhang, L. Wang, H. Fu and D. Zhao, *J. Am. Chem. Soc.*, 2014, **136**, 9280-9283.
24 H. Pan, Y. Zhang, V. B. Shenoy and H. Gao, *J. Phys. Chem. C*, 2011, **115**, 12224-12231.
25 C. Yang, Z. Wang, T. Lin, H. Yin, X. Lü, D. Wan, T. Xu, C. Zheng, J. Lin, F. Huang, X. Xie and M. Jiang, *J. Am. Chem. Soc.*, 2013, **135**, 17831-17838.
26 A. Naldoni, M. Allieta, S. Santangelo, M. Marelli, F. Fabbri, S. Cappelli, C. L. Bianchi, R. Psaro and V. D. Santo, *J. Am. Chem. Soc.*, 2012, **134**, 7600-7603.
27 S. Myung, M. Kikuchi, C. S. Yoon, H. Yashiro, S. Kim, Y. Sun and B. Scrosati, *Energy Environ. Sci.*, 2013, **6**, 2609-2614.
28 Z. Wang, B. Wen, Q. Hao, L. Liu, C. Zhou, X. Mao, X. Lang, W. Yin, D. Dai, A. Selloni and X. Yang, *J. Am. Chem. Soc.*, 2015, **137**, 9146-9152.
29 H. Zhang and J. F. Banfield, *Chem. Rev.*, 2014, **114**, 9613-9644.
30 W. Li, F. Wang, Y. Liu, J. Wang, J. Yang, L. Zhang, A. A. Elzatahry, D. Al-Dahyan, Y. Xia and D. Zhao, *Nano Lett.*, 2015, **15**, 2186-2193.
31 Y. Yang, L. Qu, L. Dai, T. S. Kang and M. Durstock, *Adv. Mater.*, 2007, **19**, 1239-1243.
32 W. Zhou, F. Sun, K. Pan, G. Tian, B. Jiang, Z. Ren, C. Tian and H. Fu, *Adv. Funct. Mater.*, 2011, **21**, 1922-1930.
33 Z. Zheng, B. Huang, J. Lu, Z. Wang, X. Qin, X. Zhang, Y. Dai and M. H. Whangbo, *Chem. Commun.*, 2012, **48**, 5733-5735.
34 T. L.Thompson and J. T. Yates, *Chem. Rev.*, 2006, **106**, 4428-4453.
35 Y. Deng, J. Wei, Z. Sun and D. Zhao, *Chem. Soc. Rev.*, 2013, **42**, 4054-4070.

36 W. Li, J. Yang, Z. Wu, J. Wang, B. Li, S. Feng, Y. Deng, F. Zhang and D. Zhao, *J. Am. Chem. Soc.*, 2012, **134**, 11864-11867.
37 A. Danon, K. Bhattacharyya, B. K. Vijayan, J. Lu, D. J. Sauter, K. A. Gray, P. C. Stair and E. Weitz, *ACS Catal.*, 2012, **2**, 45-49.
38 A. Teleki and S. E. Pratsinis, *Phys. Chem. Chem. Phys.*, 2009, **11**, 3742-3747.
39 G. Wang, H. Wang, Y. Ling, Y. Tang, X. Yang, R. C. Fitzmorris, C. Wang, J. Z. Zhang and Y. Li, *Nano Lett.*, 2011, **11**, 3026-3033.
40 L. Liu, P. Y. Yu, X. Chen, S. S. Mao and D. Z. Shen, *Phys. Rev. Lett.*, 2013, **111**, 065505.
41 X. Chen, D. Zhao, K. Liu, C. Wang, L. Liu, B. Li, Z. Zhang and D. Shen, *ACS Appl. Mater. Interfaces*, 2015, **7**, 16070-16077.
42 F. Zuo, K. Bozhilov, R. J. Dillon, L. Wang, P. Smith, X. Zhao, C. Bardeen and P. Feng, *Angew. Chem. Int. Ed.*, 2012, **51**, 6223-6226.
43 N. Liu, C. Schneider, D. Freitag, M. Hartmann, U. Venkatesan, J. Müller, E. Spiecker and P. Schmuki, *Nano Lett.*, 2014, **14**, 3309-3313.
44 N. Liu, C. Schneider, D. Freitag, U. Venkatesan, V. R. R. Marthala, M. Hartmann, B. Winter, E. Spiecker, A. Osvet, E. M. Zolnhofer, K. Meyer, T. Nakajima, X. Zhou and P. Schmuki, *Angew. Chem. Int. Ed.*, 2014, **53**, 14201-14205.
45 J. Huo, Y. Hu, H. Jiang and C. Li, *Nanoscale*, 2014, **6**, 9078-9084.
46 M. Anpo, M. Che, B. Fubini, E. Garrone, E. Giamello and M. C. Paganini, *Top. Catal.*, 1999, **8**, 189-198.
47 Y. Hu, N. Berdunov, C. Di, I. Nandhakumar, F. Zhang, X. Gao, D. Zhu and H. Sirringhaus, *ACS Nano*, 2014, **8**, 6778-6787.
48 A. Liscio, V. Palermo and P. Samorì, *Acc. Chem. Res.*, 2010, **43**, 541-550.
49 A. K. Sinensky and A. M. Belcher, *Nat. Nanotechnol.*, 2007, **2**, 653-659.
50 S. U. Nanayakkara, G. Cohen, C. S. Jiang, M. J. Romero, K. Maturova, M. Al-Jassim, J. van de Lagemaat, Y. Rosenwaks and J. M. Luther, *Nano Lett.*, 2013, **13**, 1278-1284.
51 X. Zhang, Y. Lin, D. He, J. Zhang, Z. Fan and T. Xie, *Chem. Phys. Lett.*, 2011, **504**, 71-75.
52 L. Kronik and Y. Shapira, *Surf. Sci. Rep.*, 1999, **37**, 1-206.
53 H. Zhang, G. Wang, D. Chen, X. Lv and J. Li, *Chem. Mater.*, 2008, **20**, 6543-6549.
54 Y. Hou, F. Zuo, A. Dagg and P. Feng, *Angew. Chem. Int. Ed.*, 2013, **52**, 10179-10189.
55 C. Mao, F. Zuo, Y. Hou, X. Bu and P. Feng, *Angew. Chem. Int. Ed.*, 2014, **53**, 10485-10489.
56 C. S. Enache, J. Schoonman and R. Van De Krol, *J. Electroceram.*, 2004, **13**, 177-182.

Graphical Abstract

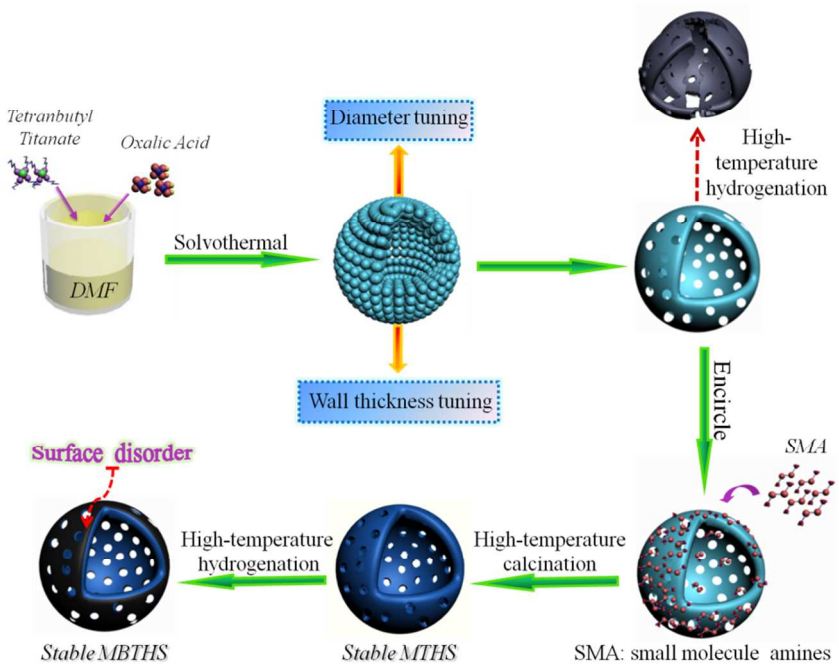

Stable mesoporous black TiO_2 hollow spheres with controllable diameter, wall thichness and narrow bandgap are fabricated *via* facile strategy of template-free solvothermal approach combined with small amine molecules encircling strategy and subsequent high-temperature hydrogenation, and exhibit excellent solar-driven photocatalytic hydrogen evolution due to the high crystallinity, integrated hollow structure, Ti^{3+} in frameworks and surface disorders.